Journal of
Synchrotron
Radiation

ISSN 0909-0495

Received 23 April 2007
Accepted 12 September 2007

Refraction and scattering of X-rays in analyzer-based imaging

Heikki Suhonen,[a]* Manuel Fernández,[b,c] Alberto Bravin,[b] Jani Keyriläinen[b] and Pekka Suortti[a,b]

[a]Department of Physical Sciences, PL 64, FIN-00014 Helsinki University, Finland, [b]Bio-medical Beamline ID17, European Synchrotron Radiation Facility, BP 220, F-38043 Grenoble, France, and [c]Inserm, U836(6), Grenoble Institute of Neurosciences, ESRF, BP 220, F-38043 Grenoble, France. E-mail: heikki.suhonen@helsinki.fi

A new algorithm is introduced for separation of the scattered and non-scattered parts of a monochromatic and well collimated synchrotron radiation beam transmitted through a sample and analyzed by reflection from a perfect crystal in the non-dispersive setting. The observed rocking curve is described by the Voigt function, which is a convolution of Lorentzian and Gaussian functions. For the actual fitting, pseudo-Voigtians are used. The fit yields the scaled integrated intensity (the effect of absorption), the center of the rocking curve (the effect of refraction), and the intensity of the transmitted beam is divided into the scattered and non-scattered parts. The algorithm is tested using samples that exhibit various degrees of refraction and scattering. Very close fits are achieved in an angular range that is 15 times the full width at half-maximum of the intrinsic rocking curve of the analyzer. The scattering part has long tails of Lorentzian shape owing to the 'long-slit geometry' of the set-up. Quantitative images of absorption, refraction and scattering are constructed and compared with results of earlier treatments. The portion of scattering and the second moment of the observed rocking curve both increase linearly with the sample thickness and yield identical maps of the effects of scattering. The effects of refraction are calculated using the geometrical optics approximation, and a good agreement with experiment is found. The fits with reduced number of data points (minimum number is five) yield closely the same results as fits to the full data set.

Keywords: diffraction enhanced imaging; analyzer-based imaging; X-ray scattering; Voigtian function.

1. Introduction

The interaction of X-rays with matter can be summarized by the refractive index,

$$n = 1 - \delta + i\beta. \quad (1)$$

The real part δ corresponds to the phase change of the resultant transmitted wave, and the imaginary part β to the decrease of its amplitude. For X-rays of a few tens of keV energy propagating in a low-Z medium the relative change in the phase may be several orders of magnitude larger than the relative change in the amplitude. For imaging of soft tissues the variation of δ is potentially a much stronger source of contrast than the variation of β.

One of the methods of observing the effects of local variation in δ by analyzing the transmitted beam using a perfect crystal is called diffraction enhanced imaging (DEI) (Chapman *et al.*, 1997) or analyzer-based imaging (ABI) (Pagot *et al.*, 2003). The experimental set-up is basically that of a Bonse–Hart camera (Bonse & Hart, 1966), although often only single reflections at the monochromator and analyzer are used. When a pencil beam traverses the sample its propagation direction may change owing to refraction, and various scattering distributions are created along the path of the beam. The angular distribution of the transmitted beam in the plane of diffraction is recorded by rocking the analyzer crystal, so that the observed intensity is proportional to the convolution of the actual angular distribution of the transmitted beam and the rocking curve of the analyzer crystal.

In its original form, DEI is performed by tuning the analyzer to reflect at half-height on the opposite sides [low (L) and high (H)] of the analyzer rocking curve. Small changes in the propagation direction owing to refraction are converted to intensity changes at the steep slope of the rocking curve. The refraction angle and the apparent absorption are solved from a first-order Taylor expansion for the intensities I_L and I_H.

However, this method ignores the presence of ultra-small-angle X-ray scattering (USAXS) in the transmitted beam. In such a case the width of the rocking curve is increased from the intrinsic value, and the slope is decreased. The difference between I_L and I_H is reduced, which would be interpreted as lowered amounts of refraction. Thus, the presence of USAXS affects both the refraction angle and apparent absorption images. However, the enhanced contrast reveals details of the sample morphology and is often sufficient for a qualitative interpretation of the images. The method has been used for imaging soft tissues, and particularly the images acquired at the maximum of the intrinsic rocking curve (top position) make visible small objects owing to combined effects of refraction and scatter rejection (Hasnah *et al.*, 2002; Zhong *et al.*, 2000; Keyriläinen *et al.*, 2005; Bravin *et al.*, 2007).

It is obvious that the scattering contribution and the effects of refraction should be separated in quantitative analysis of the analyzer-based images. The refraction angle in the plane of diffraction is proportional to the gradient of the phase φ in that direction, $\Delta\theta = -(\lambda/2\pi)(\partial\varphi/\partial z)$, where λ is the X-ray wavelength. Mapping of the refraction angle gives access to small variations of the object density, revealing tissue morphology on the level that is determined by the spatial resolution of the detector. On the other hand, USAXS (and SAXS, which is partly outside the angular window of the analyzer) arises from electron density variations at the molecular and above-molecular level. It has been demonstrated that the scattering patterns are 'signatures' of different tissues, and that cancer growth causes changes in the patterns (Lewis *et al.*, 2000; Fernández *et al.*, 2002, 2005). Therefore, an adequate analysis of the scattering contribution in the analyzer-based images provides essential information on the tissue structures.

Recently, several different approaches have been put forward to account for the effects of scattering in ABI. In the treatment of Oltulu *et al.* (2003), the observed angular distribution of the transmitted beam is written as a sum of distributions of the non-scattered and scattered beams, and the propagation direction of the beams may have changed owing to refraction. The angular distribution for the non-scattered beam is that of the intrinsic rocking curve of the analyzer, and the distribution of the scattered beam is given as a convolution of the intrinsic rocking curve and an appropriate function for the scattering distribution. Gaussian approximations are used throughout in this treatment. In another approach, the intrinsic rocking curve is convolved by an impulse response function of the sample explicitly (Wernick *et al.*, 2003) or implicitly (Pagot *et al.*, 2003). The observed rocking curve is characterized by the zeroth moment (effects of attenuation), the first moment (effects of refraction) and the second moment (effects of USAXS), and parametric images are constructed pixel-by-pixel. Multiple-image radiography (MIR) has been reformulated using the radiative transport description of beam propagation (Khelashvili *et al.*, 2006). One important outcome of this treatment is that all three images correspond to line integrals of the respective parameters, which justifies analyzer-based computed tomography imaging. For *in vivo* applications the number of images, *i.e.* the number of working points along the analyzer rocking curve, should be kept minimum. The original DEI method has been extended by adding a second-order term to the Taylor expansion for the rocking curve, and images of attenuation, refraction and scattering are derived from three measurements only (Rigon *et al.*, 2003, 2007; Chou *et al.*, 2007).

The present treatment is a generalization of the first approach (Oltulu *et al.*, 2003), but it also facilitates a quantitative comparison with the results of MIR. The basic idea is to develop an accurate description of the observed rocking curve by analytic functions, which represent the sum of the non-scattered and scattered beams or the convolution of the two. The use of analytical functions has certain advantages. First, a small number of data points along the rocking curve may be sufficient for an adequate fit. Second, different derived quantities can be calculated for further analysis, such as the parameters used in MIR. It turns out that in most cases the Gaussian presentation is not adequate, as the observed rocking curves have long tails. This is attributed to the fact that the analyzer integrates scattering in the direction perpendicular to the diffraction plane. A Gaussian excludes this part of scattering, which may be an appreciable part of the total. In this work a more general but still simple description of the scattering distribution is introduced, and images of phantoms are analyzed using this model in order to separate the effects of refraction and scattering in a consistent way.

2. Experimental set-up and intensity recording

The monochromator and analyzer form a non-dispersive pair of crystals, so that the analyzer rocking curve is the auto-correlation function of the perfect crystal rocking curve. The relative rocking angle θ is zero when the crystals are parallel, and the working point is denoted by θ_A. The effect of

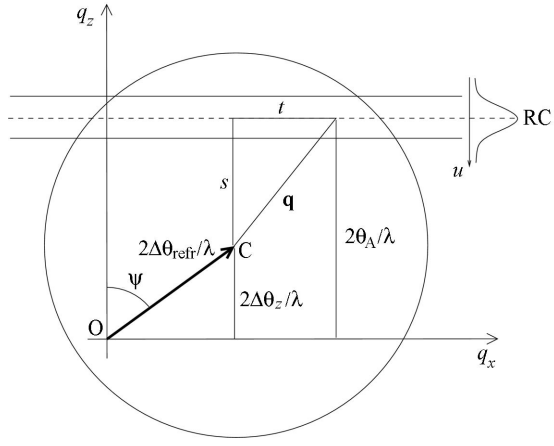

Figure 1
Refraction and scattering of a pencil beam in the scattering vector scale, $q = 2\sin(\theta)/\lambda$. The beam is deviated from O to C by refraction and a halo of scattered radiation is created, indicated by the circle. The horizontal lines indicate the 'long receiving slit' of the analyzer crystal rocking curve RC centered at $2\theta_A/\lambda = 2\Delta\theta_z/\lambda + s$.

refraction is shown in Fig. 1. The angle of incidence at the analyzer is

$$\theta = \theta_A - \cos\psi\ \Delta\theta_{refr} = \theta_A - \Delta\theta_z. \quad (2)$$

Here $\Delta\theta_{refr}$ is the deviation of a pencil beam owing to refraction, and ψ is the azimuth angle of the refracted beam. Only the component $\Delta\theta_z$ affects the angle of diffraction at the analyzer.

We consider the general case where the object is illuminated by a uniform beam and the transmitted beam is recorded by a two-dimensional pixel detector, *e.g.* by a CCD camera or imaging plate. For understanding the intensity recording, typical spatial and angular dimensions are considered. The angular opening of a detector pixel, as seen from the sample, is about 20 μrad in the present experiment. The X-ray energy is 51.5 keV, *i.e.* the wavelength λ is 0.0241 nm, and so USAXS is confined to a range smaller than 20 μrad, but SAXS extends to the mrad regime.

Scattered radiation forms a halo or 'dress' around the pencil beam traversing the sample, as shown in Fig. 1. In the following, axial symmetry of scattering is assumed in order to keep the functional forms sufficiently simple. The analyzer is a 'long slit' in the terminology of SAXS, meaning that the angular slit is open in the direction perpendicular to the diffraction plane so that scattering at fixed s is integrated in the lateral direction (t in Fig. 1). The projection of the scattering vector on the diffraction plane is

$$s = 2\sin\theta/\lambda \simeq 2\big(\theta_A - \Delta\theta_z\big)/\lambda. \quad (3)$$

The scattering vector position $\mathbf{q}$ in the 'slit' opening is indicated by t in the direction perpendicular to the diffraction plane, and by u in that plane. The observed intensity, integrated over the lateral opening of the detector, is (Feigin & Svergun, 1987)

$$I(s) = \int\int R(u)\, I\left\{\left[t^2 + (s-u)^2\right]^{1/2}\right\} \mathrm{d}t\, \mathrm{d}u, \quad (4)$$

where $R(u)$ is the reflectivity of the analyzer crystal in the scattering vector scale. Integration over t gives the 'long slit' intensity at $s - u$, $I_\infty(s-u)$, so that

$$I(s) = \int R(u)\, I_\infty(s-u)\, \mathrm{d}u = R(s) \otimes I_\infty(s), \quad (5)$$

where $\otimes$ indicates convolution. It must be noted here that owing to the 'long slit' geometry of the two-crystal (Bonse–Hart) set-up there is no clear separation between USAXS and SAXS. At the detector, the refracted pencil beam and USAXS fall on the same pixel, but the contribution from SAXS spreads out in the lateral direction to the neighboring pixels.

The radiation scattered away from the incident beam and not recorded by the detector is termed the absorption loss. Evidently this depends on the scanning range of the analyzer and the lateral opening of the beam. As argued above, the refracted beam, USAXS and some part of SAXS are detected, so that the attenuation factor is

$$\exp(-\mu T) = \int I(\theta_A)\, \mathrm{d}\theta_A \,/\, \int I_0 R_{int}(\theta_A)\, \mathrm{d}\theta_A, \quad (6)$$

where I_0 is the incident intensity (flux per pixel) from the monochromator, and $R_{int}(\theta_A)$ is the intrinsic rocking curve of the analyzer, when there is no sample.

Following Oltulu *et al.* (2003), the transmitted beam is divided into the non-scattered refracted beam and the halo of scattering around it. The observed reflectivity at the rocking angle θ_A is

$$R_1(\theta_A) \equiv I(\theta_A)/I_0 = \exp(-\mu T) \int [\xi\delta(\theta) + (1-\xi)F_1(\theta)] \times R_{int}\big[\theta - \big(\theta_A - \Delta\theta_z\big)\big]\, \mathrm{d}\theta. \quad (7)$$

The δ function counts for the refracted beam, and F_1 for the associated scattering. Both functions are normalized to unity, and the intrinsic rocking curve is convolved by the weighed sum of these functions. The maximum of $R(\theta_A)$ is at $\theta_A = \Delta\theta_z$. It has already been mentioned that R_{int} is the autocorrelation function of the reflectivity curve.

The corresponding equation in the treatments where the incident distribution is convolved by the scattering distribution (Pagot *et al.*, 2003; Wernick *et al.*, 2003) is

$$R_2(\theta_A) = \exp(-\mu T) \int F_2(\theta)\, R_{int}\big[\theta - \big(\theta_A - \Delta\theta_z\big)\big]\, \mathrm{d}\theta, \quad (8)$$

where $F_2(\theta)$ is normalized to unity.

3. Functional form of scattering

When the axially symmetrical scattering distribution $I(q)$ around the refracted beam is observed through the 'long slit' of the analyzer crystal the distribution is smeared. The effect of smearing can be calculated for given analytical forms of $I(q)$. In general, the contribution of the tails of $I(q)$ are enhanced in $I_\infty(s)$. At sufficiently large values of q,

$$I(q) \propto q^{-p}, \quad (9)$$

where the exponent p is 4 for three-dimensional objects with a smooth surface, 2 for two-dimensional discs, 1 for one-dimensional rods, 2 or 5/3 for coils, and between 1 and 4 for different mass and surface fractals (Feigin & Svergun, 1987; Schmidt, 1991). Integration over the 'long slit' gives

$$I_\infty(s) \propto s^{-(p-1)}, \quad (10)$$

except in the case $p = 1$. At small values of q, where Guinier's law applies (Guinier & Fournet, 1955), $I(q)$ is approximately Gaussian, and also the corresponding $I_\infty(s)$ remains Gaussian. The observed intensity is a combination of the small-q and large-q contributions, so that a functional form that has a pronounced peak and long tails is to be found for $F_1(\theta)$ and $F_2(\theta)$.

The main application of ABI is tissue imaging, and therefore we look for a functional form that approximates SAXS from tissues. The actual form of the SAXS intensity depends on the sample, but in human breast tissue samples an approximate q^{-3} behavior was found in many cases (Fernández *et al.*, 2002, 2005). It is expected that the total scattering seen by a detector pixel changes from the Gaussian to the Lorentzian shape when the analyzer angle $\theta = \theta_A - \Delta\theta_z$ is increased. This behavior can be described by a single

function called Voigtian (V), which is a convolution of a Gaussian (G) and a Lorentzian (L),

$$\mathrm{V}_s(\theta) = \mathrm{G}_s(\theta) \otimes \mathrm{L}_s(\theta). \tag{11}$$

It will be seen that use of these functions makes the mathematical formulation simple, but still versatile.

In the following we start from the first treatment (Oltulu *et al.*, 2003), in order to separate the non-scattered (refracted) and scattered contributions of the detected beam. Dropping the argument $\theta = \theta_\mathrm{A} - \Delta\theta_z$ and writing $R_\mathrm{int}(\theta) = \mathrm{V}_0(\theta)\omega_\mathrm{int}$, where ω_int is the integrated reflectivity of the analyzer without a sample, the observed reflectivity from (7) is written as

$$\begin{aligned} R_1(\theta_\mathrm{A}) &= \exp(-\mu T)\omega_\mathrm{int}\left[\xi \mathrm{V}_0 + (1-\xi)\mathrm{V}_0 \otimes \mathrm{V}_s\right] \\ &= \exp(-\mu T)\omega_\mathrm{int}\left[\xi \mathrm{G}_0 \otimes \mathrm{L}_0 + (1-\xi)(\mathrm{G}_0 \otimes \mathrm{G}_s)\right. \\ &\quad \left. \otimes (\mathrm{L}_0 \otimes \mathrm{L}_s)\right] \\ &= \exp(-\mu T)\omega_\mathrm{int}\left[\xi \mathrm{V}_0 + (1-\xi)G_1 \otimes \mathrm{L}_1\right] \\ &= \exp(-\mu T)\omega_\mathrm{int}\left[\xi \mathrm{V}_0 + (1-\xi)\mathrm{V}_1\right]. \end{aligned} \tag{12}$$

The functions G, L and V are normalized to unity, and their centers are at $\Delta\theta_z$. The simplicity of the result is due to the fact that the convolution of two Gaussians is a Gaussian, and the convolution of two Lorentzians is a Lorentzian. The properties of the functions are summarized in the following section. In the corresponding equation in the second treatment (Pagot *et al.*, 2003; Wernick *et al.*, 2003), the sum within the brackets is replaced by just one Voigtian, $\mathrm{V}_2 = \mathrm{V}_0 \otimes \mathrm{V}_s$, so that the observed rocking curve is given by

$$R_2(\theta_\mathrm{A}) = \exp(-\mu T)\omega_\mathrm{int}\mathrm{V}_0 \otimes \mathrm{V}_s. \tag{13}$$

4. Voigt and pseudo-Voigt functions

The Voigt function has been used in many fields of research as a versatile description of observed peaked distributions. In particular, the Voigt function was introduced for the profile analysis of powder diffraction data (Langford, 1978; Suortti *et al.*, 1979) (see also Snyder *et al.*, 1999). In practice, the actual Voigtian is often replaced by the so-called pseudo-Voigtian (pV), which approximates the normalized real Voigtian by a weighted sum of normalized Lorentzian and Gaussian functions (Wertheim *et al.*, 1974). The properties of these functions are summarized in the following.

The normalized Gaussian and Lorentzian functions are

$$\mathrm{G}(\theta) = \frac{1}{\sigma\sqrt{2\pi}}\exp\left(-\theta^2/2\sigma^2\right), \tag{14}$$

$$\mathrm{L}(\theta) = \frac{a}{\pi(a^2+\theta^2)}. \tag{15}$$

The Gaussian is fully determined either by the standard deviation σ or by the full width at half-maximum, FWHM = $2\sigma(2\ln 2)^{1/2} = 2.3548\sigma$, and the Lorenzian by FWHM = $2a$. The corresponding integral breadths are $\beta_\mathrm{G} = \sigma(2\pi)^{1/2} = 2.5066\sigma$ and $\beta_\mathrm{L} = \pi a = 3.1416a$. The normalized Voigtian is determined by β_G and β_L (Suortti *et al.*, 1979),

$$\mathrm{V}(\theta) = \frac{1}{\beta_\mathrm{G}}\Re\left(\Phi\left\{\left[\left(\pi/\beta_\mathrm{G}\right)^{1/2}\right]\theta + iy\right\}\right), \tag{16}$$

where $y = \beta_\mathrm{L}/(\pi\beta_\mathrm{G})^{1/2}$, and $\Re[\Phi(z)]$ is the real part of the complex error function,

$$\Phi(z) = \exp\left(-z^2\right)\mathrm{erfc}(-iz). \tag{17}$$

The relative importance of the Lorentzian and Gaussian functions are given by y; the value $y = 0$ corresponds to a pure Gaussian, and the value $y = \infty$ to a pure Lorentzian function. In the pseudo-Voigtian presentation (subscript pV) the FWHM of both components is that of the real Voigtian, $2w_\mathrm{V}$, and the relative weights are given by factor η,

$$\mathrm{V} = \eta L_\mathrm{pV} + (1-\eta)\mathrm{G}_\mathrm{pV}. \tag{18}$$

There are approximate expressions for $w_\mathrm{L}/w_\mathrm{V}$ and $w_\mathrm{G}/w_\mathrm{V}$, given as functions of the weight factor η (Thompson *et al.*, 1987).

With the pseudo-Voigtian presentation the normalized intensity distribution from (12) is

$$\begin{aligned} R_1(\theta_\mathrm{A})/\omega_\mathrm{int} = \exp(-\mu T)\{&\xi\left[\eta_0 L_{0,\mathrm{pV}} + (1-\eta_0)\mathrm{G}_{0,\mathrm{pV}}\right] \\ &+(1-\xi)\left[\eta_1 L_{1,\mathrm{pV}} + (1-\eta_1)\mathrm{G}_{1,\mathrm{pV}}\right]\}. \end{aligned} \tag{19}$$

The corresponding expression in the second treatment is

$$R_2(\theta_\mathrm{A})/\omega_\mathrm{int} = \exp(-\mu T)\left[\eta_2 L_{2,\mathrm{pV}} + (1-\eta_2)\mathrm{G}_{2,\mathrm{pV}}\right]. \tag{20}$$

These are the actual working formulae, which are used in the next section to resolve the observed intensity to the non-scattered (refracted) and scattered components, or to derive parameters describing these components. The weight factor for scattering in the first case (19) may be written as $1 - \xi = 1 - \exp(-\chi T)$, where χ is the small-angle scattering coefficient (extinction coefficient) per unit length of the beam path. In the second case (20) the scattering contribution is not measured by a weight factor, but by its standard deviation $\sigma_\mathrm{sc} = (\sigma^2_\mathrm{obs} - \sigma^2_\mathrm{int})^{1/2}$, which is calculated from the second moments of the observed intensity distributions.

5. Refracting and scattering phantoms

The phantoms used in the experiment resembled the one used by Oltulu *et al.* (2003), but several additional components were included: there was a strip of 1–11 layers of paper, so that the thickness increased stepwise from 0.1 mm to 1.1 mm, silver behenate powder, dry 100 nm-diameter PMMA spheres, and a Lucite rod of diameter 10 mm across the paper strips. These components were mounted in aluminium sample holders (see Fig. 2). Radial scattering patterns of the different components are shown in Fig. 2(*b*). Cellulose fibers are hierarchical structures that cover many length scales, so that strong SAXS is expected from paper (Fengel & Wegener, 1984). Silver behenate powder is often used for calibration of the angular scale in SAXS experiments, because the lattice constant is large (5.84 nm), and there are distinct Bragg reflections at small scattering angles. The SAXS pattern from independent PMMA spheres can be calculated, and it is used for intensity

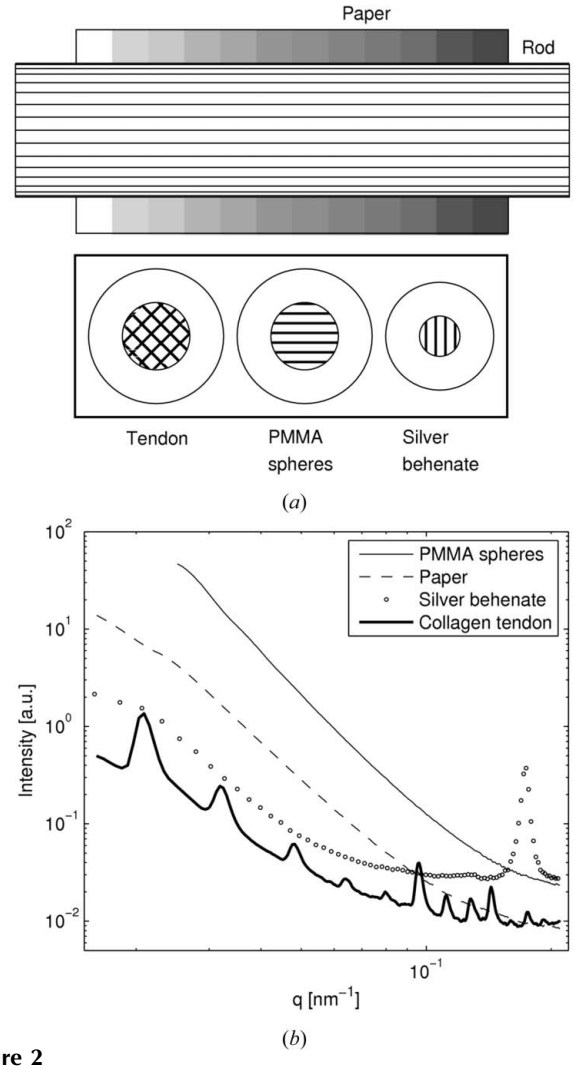

Figure 2
(*a*) Ensemble of phantoms at the sample holder. These include a strip of 1–11 layers of paper, crossed by a Lucite rod of diameter 10 mm (top), and about 1 mm-thick loosely packed discs of silver behenate powder, dry PMMA spheres of diameter 100 nm, and ox tendon (bottom). The latter samples are contained by thin Kapton windows. (*b*) Radial SAXS patterns of the components. The intensities are scaled to correspond to approximately the same sample thicknesses.

calibration and testing of the SAXS cameras. The Lucite rod causes strong effects of refraction near the edges.

6. Experimental details

The phantoms were imaged at the Medical beamline (ID17) of the European Synchrotron Radiation Facility. The optics hutch is situated at 145 m from the source, which is a 21-pole wiggler with 0.6 T field at 60 mm gap. A double-Laue Si(111) pre-monochromator was used to separate a relatively broad ($\Delta E/E > 10^{-4}$) energy band at 51.5. keV. The beam was shaped by slits to a fan of 80 mm × 1 mm [horizontal (H) × vertical (V)].

The Si(333) imaging monochromator reduced the relative energy band to less than 10^{-5}, and the analyzer was an identical crystal in non-dispersive setting (Fig. 3). The phantom

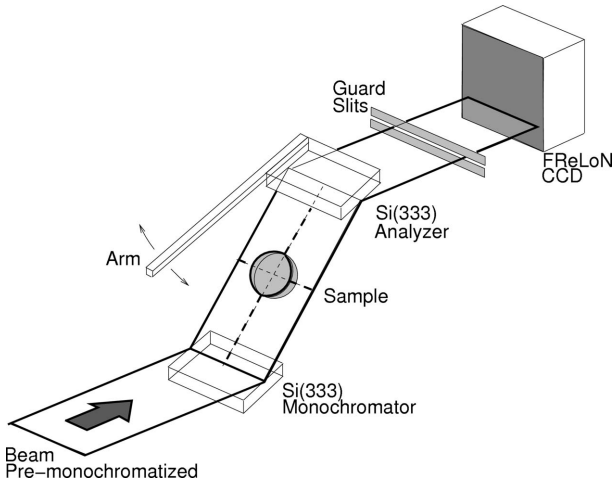

Figure 3
Perspective drawing of the DEI set-up. The Si(333) monochromator reflects a narrow band of energies at 51.5 keV. The beam dimensions are 80 mm × 1 mm (H × V). The analyzer crystal is identical to the monochromator. The pixel size of the FReLoN detector is 47 μm.

was situated approximately half way between the monochromator and the analyzer, and the phantom was scanned vertically through the beam. A fast-readout low-noise (FReLoN) CCD camera with tapered fiber optics was used in the so-called pipeline mode (Bravin *et al.*, 2003; Coan *et al.*, 2006). The pixel size of the detector was 47 μm, and the distance from the analyzer was about 2.2 m. Scanning was synchronized with readout of the detector, and a rotating chopper was used to stop the beam during readout in order to reduce the detector noise (Renier *et al.*, 2005).

The analyzer crystal is detuned from the maximum transmission (top) position by a piezo-electric drive acting on a 500 mm-long lever arm. The angular resolution is about 0.1 μrad. The scanning stage was separated from the monochromator–analyzer mount, which was placed on a vibration-damped table. Even with these precautions, some high-frequency noise (in comparison with the acquisition time) was transmitted, and there was a slow drift in the angular position of the analyzer. The reflectivity or rocking curve of the analyzer was measured in 0.2 to 1.0 μrad steps in the range ±12 μrad around the top position.

The intrinsic rocking curve $R_{\rm int}$ is measured without the sample. The experimental points and the pV fit are shown in Fig. 4. The background is negligible, but the rocking curve has tails that are not accounted for by a Gaussian form only; in fact, the parameter $\eta_0 = 0.78$ indicates a substantial Lorentzian contribution. Presumably this is due to thermal diffuse scattering (TDS) from the analyzer crystal. TDS increases at high X-ray energies, where the penetration depth controlled by absorption is much larger than the extinction distance in Bragg reflection. The fitted curve of $R_{\rm int}$ is used in the analysis to describe the non-scattered beam transmitted through the sample.

The total area of the samples in the regions of interest was about 26 cm^2, so the image field to be analyzed consisted of more than 10^6 pixels, and the field was recorded at 30–50

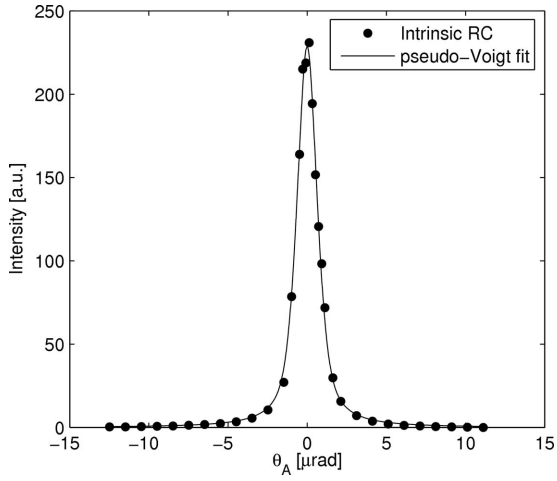

Figure 4
The measured intrinsic rocking curve of the analyzer (points), and a pseudo-Voigtian fit. The FWHM is 1.48 μrad and the Lorentzian weight $\eta_0 = 0.78$ is due to the substantial tails of the rocking curve.

analyzer settings. The images were normalized to the white field without the sample to correct for the effects of the non-uniform intensity of the incident beam. During data acquisition, the analyzer angle drift was monitored by recording the parts of the beam that were not intercepted by the sample. An algorithm was introduced for calculation of the actual working point θ_A, and the observed intensity values were assigned accordingly. A fitting routine based on (19) was applied at each pixel, so that maps of various parameters were constructed, and these correspond to refraction, absorption and scattering images of the samples. There are only five parameters to be optimized in fitting (19) to the observed scaled intensities $I(\theta_A)/I_0\omega_{int} = R(\theta_A)/\omega_{int}$. These parameters are the refraction angle $\Delta\theta_z$, the absorption factor $\exp(-\mu T)$, the parameter ξ, which gives the relative integrated intensity of the non-scattered (refracted) beam, $\Gamma = 2w_V$, which is the Voigtian FWHM of the scattered intensity, and the mixing parameter η_1 in the pseudo-Voigt representation. Another fitting routine based on (20) was used in selected areas for comparison of the different approaches. Fitting of (20) does not separate ξ, η and η_1, so that the fitting parameters are $\Delta\theta_z$, $\exp(-\mu T)$, Γ and η_2.

7. Results and discussion

7.1. Paper and Lucite rod

The fitting procedure based on (19) should be able to separate the contributions of the non-scattered and scattered beams to the total transmitted beam, which is recorded by the analyzer and detector. The procedure was tested with the phantom that consisted of 1–11 layers of paper, and was crossed by the 10 mm Lucite rod. It is expected that the attenuation increases with the layer thickness T as $\exp(-\mu T)$, where μ is the linear attenuation coefficient owing to photoelectric absorption and elastic and inelastic scattering that is not transmitted by the analyzer. The integrated scattering signal per pixel, on the other hand, should depend on T as follows, $J_{sc}(T) = J_0\sigma_{sc}T\exp(-\mu T)$, where σ_{sc} is the scattering coefficient per unit path length, and J_0 is the incident flux per pixel. SAXS intensity spreads to neighboring pixels, but this loss of intensity is compensated by scattering from other parts of the incident beam.

The working formula (19) was written in a short-hand notation as

$$R(\theta_A)/\omega_{int} = \exp(-\mu T)\big[\xi R_{int} + (1-\xi)R_{sc}\big]. \qquad (21)$$

The intrinsic rocking curve R_{int}, which describes the non-scattered (but probably refracted) beam, is already given by a pseudo-Voigtian V_0, and now a similar fit is used for the scattered part R_{sc},

$$R_{sc} = \eta_1 L_{1,pV} + (1-\eta_1)G_{1,pV}. \qquad (22)$$

In addition to the center shift owing to refraction, the fitting parameters in (21) and (22) are $\exp(-\mu T)$, ξ, η_1 and the FWHM Γ of the Voigtian.

The overall results of the fitting procedure are described first, and mapping absorption, refraction and scattering are discussed separately. A single pseudo-Voigtian function was fitted to the observed rocking curve, to obtain the peak position and an initial estimate on the width. The shape of the scattered pseudo-Voigtian was then optimized by a Nelder–Mead simplex search (Press *et al.*, 2002) for the parameters η and Γ. For each trial value of η and Γ, the mixing parameter ξ and attenuation $\exp(-\mu T)$ were optimized by a separate Nelder–Mead simplex search for the best linear combination of the intrinsic and scattering curves. This allowed the attenuation and the amount of scattering to be optimized independently of the scattering shape.

The scattering part R_{sc} should retain its shape independently of the paper thickness, so that Γ and η_1 should be constant, unless there are substantial multiple-scattering or cumulative effects of refraction. An example of the pV curves fitted to the observations is shown in Fig. 5(*a*). Figs. 5(*b*) and 5(*c*) show that R_{sc} is not properly separated when its contribution is small. The FWHM of R_{sc} increases slightly with paper thickness to more than three times the intrinsic FWHM, but the Lorentzian tails of R_{sc} become visible only gradually. The parameters Γ and η_1 are constrained to the asymptotic values shown in the figures, and these are used in the attenuation, refraction and scattering maps discussed later in this section.

7.2. Silver behenate and PMMA

The rocking curve of the beam transmitted through the sample of Ag behenate powder is shown in Fig. 6(*a*). The curve coincides almost exactly with the intrinsic rocking curve, when scaled by the attenuation factor $\exp(-\mu T) = 0.98$, indicating very weak scattering or broadening owing to refraction. This is expected from the SAXS patterns of Fig. 2, where the intensity from the powder sample is low except for the strong crystal reflection at $s = 0.171\ \mathrm{nm}^{-1}$. On the other hand, when the beam transmitted through the sample of PMMA spheres is divided according to (19), the intrinsic part is negligible, suggesting complete scattering of the incident

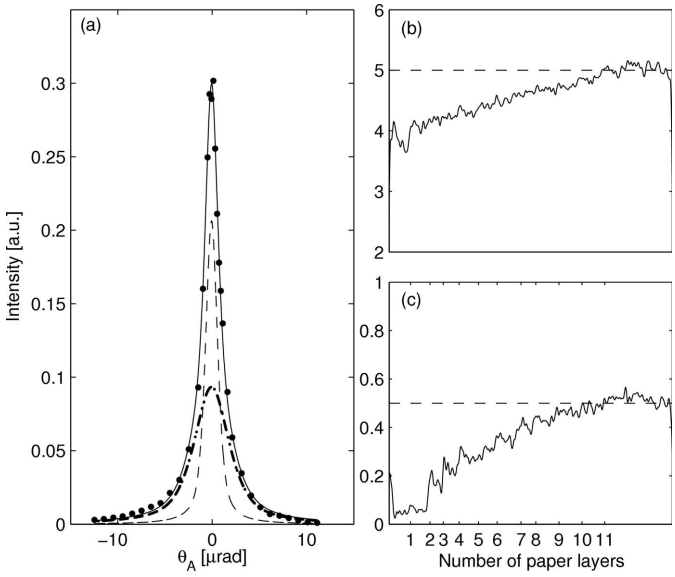

Figure 5
(*a*) The rocking-curve fit for the beam that had traversed 11 layers of paper. The contributions are the non-scattered beam (dashed line), scattered beam (dotted) and their sum (solid line). (*b*) The FWHM and (*c*) the Lorentzian weight factor η_1 as functions of the paper thickness in an unconstrained fit to (22). In subsequent fitting the values $\Gamma = 5.5$ μrad and $\eta = 0.5$ are used.

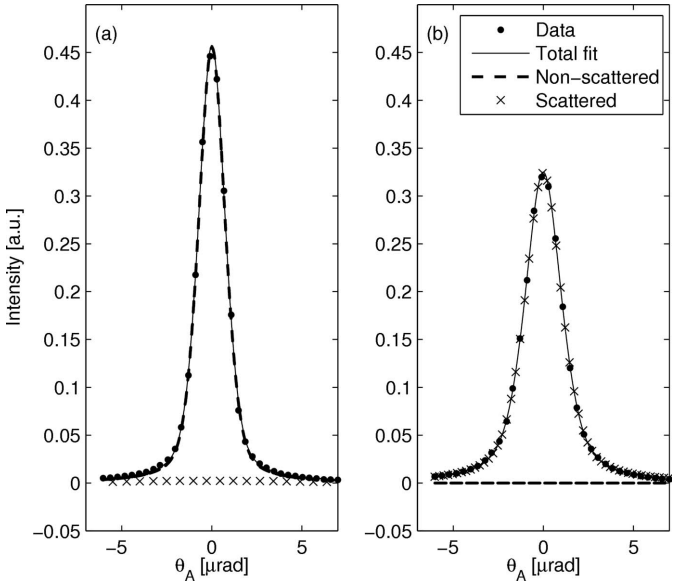

Figure 6
Pseudo-Voigtian fits to beams that have traversed a sample of silver behenate powder (*a*) and PMMA spheres (*b*).

beam (Fig. 6*b*). The FWHM is 2.45 μrad, while the FWHM of the intrinsic rocking curve is 1.48 μrad. The SAXS pattern of the PMMA sample can be calculated for independent spheres of diameter 100 nm. The result is shown in Fig. 7 on a logarithmic scale. The calculated SAXS pattern is two orders of magnitude wider than the observed rocking curve. Presumably the reason for this discrepancy is the fact that the PMMA spheres are not independent, but form closely packed powder-like granules, which have diameters of a few micrometers. The inner structure of these granules, *i.e.* the individual spheres,

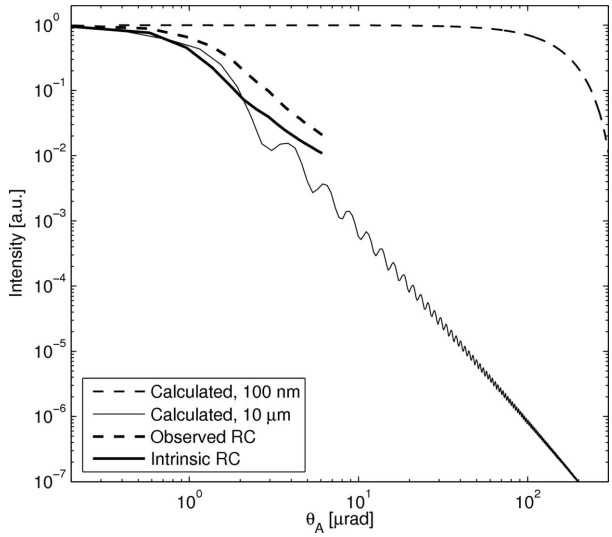

Figure 7
Calculated rocking curve for the beam scattered by PMMA spheres of diameter 100 nm (thin broken line) and 10 μm (thin solid line), together with the observed rocking curve (thick broken line) and the intrinsic rocking curve (thick solid line).

gives rise to the s^{-3} or q^{-4} behavior in the Porod regime between $q = 0.03$ and 0.1 nm^{-1}, which is seen in Fig. 2, while the width of the central peak is due to the size of the granules.

7.3. Attenuation, refraction and scattering maps

Parametric maps for the beam transmitted through the paper and Lucite part of the phantom are shown in Fig. 8. The attenuation map is shown in Fig. 8(*a*), and the bands where attenuation, refraction angle and scattering fraction are calculated are indicated by broken lines. Another image of the rod is shown in Fig. 8(*b*), which is acquired at the top position of the analyzer. The drop of intensity with increasing paper thickness is due to the scattering loss, $1 - \xi$, which is shown in Fig. 8(*c*). The effect of refraction is a strong decrease of intensity at the edges of the rod, and this is closely reproduced by calculation. The calculation is based on the geometrical optics approximation (*cf.* Keyriläinen *et al.*, 2002), which is valid when the Takagi number $(h/\lambda)^2[R_0(\theta)/R_0''(\theta)] \gg 1$; here h is the smallest discernible feature of the object, given by the detector pixel size, and R_0 is the analyzer reflectivity (Nesterets *et al.*, 2006). Extrapolating from earlier calculations for the Si(333) analyzer reflection the Takagi number is about 40 in the vicinity of the center of the Bragg reflection (Pavlov *et al.*, 2004). The agreement between the calculation and experiment demonstrates that the geometrical optics calculation is valid in the present case.

The redistribution of intensity by scattering is shown quantitatively in Fig. 8(*c*) using the parameters ξ and $\exp(-\mu T)$. The portion of the scattered radiation, $1 - \xi$, increases from 0 at zero paper thickness to 0.6 at the maximum paper thickness of 1.1 mm, while the total transmission factor $\exp(-\mu T)$ drops by a few percent only. The non-scattered and scattered parts of the transmitted beam are well separated by the Voigtian presentation, and the scattering contribution

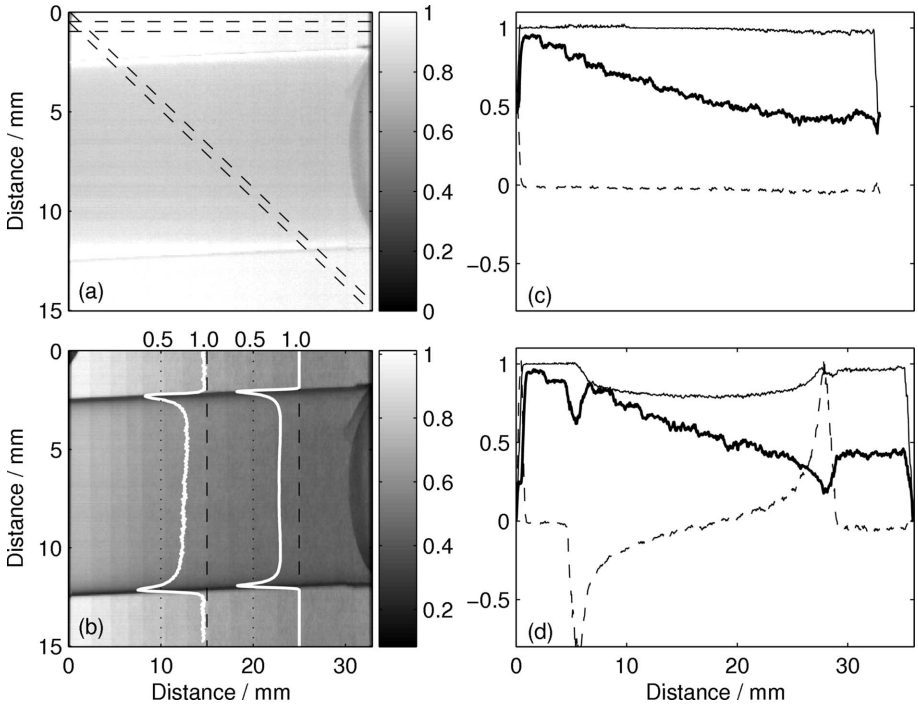

Figure 8
(*a*) Attenuation in the phantom of 0–11 paper layers plus a Lucite rod of diameter 10 mm. The thin broken lines indicate the bands where curves in (*c*) and (*d*) were calculated. (*b*) Top image of the phantom with intensity curves across the rod: experiment (left) and calculation (right). (*c*) Transmitted intensity (thin line), non-scattered portion ξ (thick line) and refraction angle (broken line) along the horizontal band in (*a*). (*d*) Transmitted intensity (thin line), refraction angle (broken line) and portion of the non-scattered beam (thick line) along the diagonal band in (*a*). For the pseudo-Voigtian fit (21) the full data set of 33 points between −12.5 μrad and +11.0 μrad are used.

follows the expected linear behavior with T. The simultaneous effects of attenuation, refraction and scattering are shown along a line that crosses the Lucite rod and the underlying layers of paper (Fig. 8*d*). The curve-fitting procedure separates absorption (mostly in the Lucite rod), the peak shift owing to refraction and the stepwise increase of scattering with the increasing thickness of the paper layer.

7.4. Minimal data set for curve fitting

It has already been mentioned that reduction of the number of working points along the rocking curve is essential, particularly for *in vivo* imaging, where the allowed radiation dose is limited. There are five parameters to be optimized in fitting the Voigt function (19) to the observed rocking curve, and four parameters in (20). The stability of the fit was tested by varying the number and location of data points on the rocking curve. Results for attenuation, the refraction angle and the portion ξ of the non-scattered beam are shown in Fig. 9 along the same line as in Fig. 8(*d*). At least in this simple case the results obtained by using the full data set are closely reproduced already with ten data points, while with five data points the separation of refraction shift and scattering portion is incomplete.

7.5. Comparison with other methods

The different methods for treatment of analyzer-based imaging data aim at separating the effects of attenuation (true absorption and scatter rejection), beam deviation owing to refraction, and scattering. The differences between the methods arise from description of the effects of scattering. The common feature is that any deviation of the observed rocking curve from the shape of the intrinsic rocking curve is assigned to scattering, although the broadening may be due to USAXS, SAXS, multiple-scattering or cumulating refraction effects. In one approach the recorded intensity is given as a sum of two parts: the non-scattered beam, which has the shape of the intrinsic rocking curve, and the scattered part (Oltulu *et al.*, 2003). In the other approach, which is now called the MIR method (Wernick *et al.*, 2003; Khelashvili *et al.*, 2006), the interaction with the sample is included in the impulse response function (per unit path length), which convolves the intrinsic rocking curve. We have called these two treatments the sum approach and convolution approach, respectively.

The present formulation is equally amenable to the sum and convolution approaches and allows for a direct comparison of the two. In order to give quantitative results the sample made of paper layers is considered, and the parameters describing the effects of scattering are compared. The parameters of attenuation and beam deviation are identical in the two approaches. In the sum approach, the degree of scattering is given by the parameter $1 - \xi$, and in the convolution approach by the second moment of the observed rocking curve minus the second moment of the intrinsic rocking curve. It was seen in Fig. 8(*c*) that $1 - \xi$ increases linearly with the sample thickness, and in the following the second moment in the pseudo-Voigtian expression (22) is considered. The second moment of the pseudo-Voigtian function is

$$\begin{aligned} \mathrm{M}_{2,\mathrm{pV}} &= \eta \mathrm{M}_{2,\mathrm{L}} + (1-\eta)\mathrm{M}_{2,\mathrm{G}} \\ &= \eta(\Gamma/\pi)\left[\theta_{\max} - (1/2)\Gamma \tan^{-1}(2\theta_{\max}/\Gamma)\right] \\ &\quad + (1-\eta)\left(2^{1/2}/8\ln 2\right)\Gamma^2. \end{aligned} \tag{23}$$

It can be seen that $\mathrm{M}_{2,\mathrm{L}}$ increases with the integration range (from $-\theta_{\max}$ to $\theta_{\max}$) so that the range must be kept finite and constant for adequate comparisons. The last two terms tend to cancel each other, and with a sufficiently large value of $\theta_{\max}$ the second moment is proportional to the FWHM Γ. Broadening owing to successive convolutions by an impulse response function that has Lorentzian shape should increase Γ linearly with paper thickness. Results may be seen in Fig. 10.

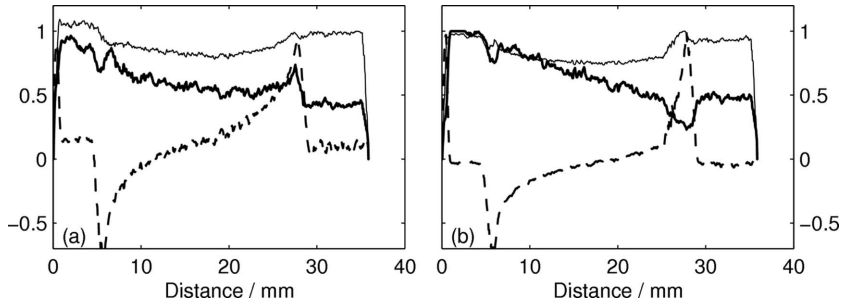

Figure 9
Transmitted intensity (thin line), refraction angle (broken line) and portion of the non-scattered beam (thick line) along the diagonal band crossing the Lucite rod and paper layers (same as in Fig. 8*d*), calculated from curves fitted to five data points (−8.6; −3.6.; −0.9; +0.1; +1.8 μrad) (*a*), and to ten data points (additional angles −6.6; −0.3; +0.5; +4.0; +10.0) (*b*) along the analyzer rocking curve.

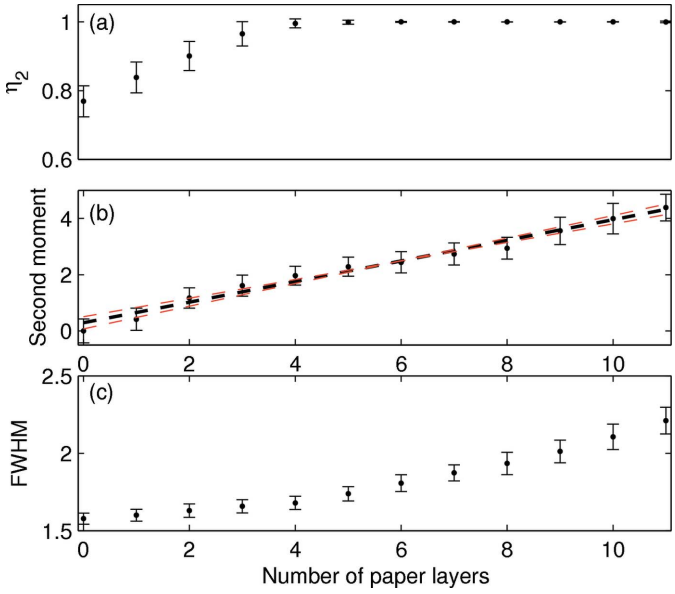

Figure 10
The Lorenzian weight factor η_2 in the pseudo-Voigtian (20), the second moment minus the second moment of the intrinsic rocking curve (broken line: linear fit), and the FWHM of the curve fitted to the rocking curve for the beam that has traversed 0–11 layers of paper.

The Lorentzian character in the pseudo-Voigtian presentation (20) is dominant and even complete at thick samples. As expected, the second moment of the total rocking curve minus that of the intrinsic rocking curve increases linearly with the sample thickness in agreement with results of earlier observations and calculations (Wernick *et al.*, 2003; Khelashvili *et al.*, 2006), and the increase of Γ is linear after four paper layers.

8. Conclusions

This study was undertaken to introduce a new parametrization of the data obtained in ABI. The method is based on fitting a simple but still versatile function to the observed rocking curve of the analyzer. The experimental set-up is essentially that of the Bonse–Hart camera in the 'long-slit' geometry, and it turns out that the rocking curves may have long tails owing to SAXS picked up in the lateral direction. An accurate description is obtained by the use of Voigt functions, which are convolutions of Lorentzian and Gaussian functions. For the actual fitting, the so-called pseudo-Voigtians are used. An even more flexible fitting function would be Pearson VII, where the asymptotic behavior of the tails can be tuned by one parameter (Pearson, 1900). This option was not studied, because the Voigt function provided an adequate description of the observed rocking curves.

The present formulation allows for a direct comparison between different treatments of the scattering contribution in the transmitted beam. It turns out that the respective parameters in the sum approach and in the convolution approach behave in the same way. There are five and four fitting parameters in the pseudo-Voigtian presentations, respectively, so that the latter approach may be favored in practical applications. The results concern scattering from paper, but these may be extended for human tissues, as both have structures in many length scales. The motivation of analyzer-based imaging is to overcome the limitations of the absorption-based methods in medical imaging, so the present observations have significance beyond the phantom studies.

Calculations for a simple object indicate that the geometrical optics approach is adequate in the present case, offering a great simplification of the general treatment of ABI (Nesterets *et al.*, 2006). In general, the image contrast is stronger in ABI than in the propagation-based imaging (PBI), although the effects overlap, and the PBI contrast is seen also in the direction perpendicular to the plane of diffraction (Pavlov *et al.*, 2004, 2005; Coan, 2006). With these reservations, extensions of the original DEI algorithm can be used to interpret the results of ABI.

This study indicates that the MIR method or its variants yield images that are similar or identical to the present results. The advantage of the curve-fitting approach is that meaningful results are obtained with their statistical accuracy with a limited number of data points along the rocking curve of the analyzer. This is important with the prospect of *in vivo* imaging, where the allowed dose is limited. It is also remarkable that the combined effects of refraction and scattering are seen in the top image. This has been exploited in imaging breast cancer samples, where important structures such as collagen strands and micro-calcifications are highlighted (Keyriläinen *et al.*, 2002; Bravin *et al.*, 2007). The present work demonstrates that it is sufficient to image the sample at a few analyzer angles and still be able to extract the scattering contribution. SAXS in particular carries information about the molecular structure of the object, and the changes in breast tissue structures have been used as indicators of cancer growth. It may be possible to combine the

morphological information from ABI with information about the molecular structures and their changes.

The authors thank the staff of the Bio-medical beamline at the ESRF for help in experiments and in analysis of data. The financial support of The Academy of Finland (project No. 210160) and the ESRF is gratefully acknowledged.

References

Bonse, U. & Hart, M. (1966). *Z. Phys.* **189**, 151–162.

Bravin, A., Fiedler, S., Coan, P., Labiche, J.-C., Ponchut, C., Peterzol, A. & Thomlinson, W. (2003). *Nucl. Instrum. Methods Phys. Res. A*, **510**, 35–40.

Bravin, A., Keyriläinen, J., Fernández, M., Fiedler, S., Nemoz, C., Karjalainen-Lindsberg, M.-L., Tenhunen, M., Virkkunen, P., Leidenius, M., von Smitten, K., Sipilä, P. & Suortti, P. (2007). *Phys. Med. Biol.* **52**, 2197–2211.

Chapman, D., Thomlinson, W., Johnston, R. E., Washburn, D., Pisano, E., Gmür, N., Zhong, Z., Menk, R., Arfelli, F. & Sayers, D. (1997). *Phys. Med. Biol.* **42**, 2015–2025.

Chou, C.-Y., Anastasio, M. A., Brankov, J. G., Wernick, M. N., Brey, E. M., Connor, D. M. Jr & Zhong, Z. (2007). *Phys. Med. Biol.* **52**, 1923–1945.

Coan, P. (2006). PhD thesis, Université Joseph Fourier, Grenoble, France.

Coan, P., Peterzol, A., Fiedler, S., Ponchut, C., Labiche, J. C. & Bravin, A. (2006). *J. Synchrotron Rad.* **13**, 260–270.

Feigin, L. A. & Svergun, D. I. (1987). *Structure Analysis by Small-Angle X-ray and Neutron Scattering.* New York: Plenum Press.

Fengel, D. & Wegener, G. (1984). *Wood: Chemistry, Ultrastructure, Reactions.* Berlin/New York: Walter de Gruyter.

Fernández, M., Keyriläinen, J., Serimaa, R., Torkkeli, M., Karjalainen-Lindsberg, M.-L., Leidenius, M., von Smitten, K., Tenhunen, M., Fiedler, S., Bravin, A., Weiss, T. M. & Suortti, P. (2005). *Phys. Med. Biol.* **50**, 2991–3006.

Fernández, M., Keyriläinen, J., Serimaa, R., Torkkeli, M., Karjalainen-Lindsberg, M.-L., Tenhunen, M., Thomlinson, W., Urban, V. & Suortti, P. (2002). *Phys. Med. Biol.* **47**, 577–592.

Guinier, A. & Fournet, G. (1955). *Small-Angle X-ray Scattering.* New York: Wiley.

Hasnah, M. O., Zhong, Z., Oltulu, O., Pisano, E., Johnston, R. E., Sayers, D., Thomlinson, W. & Chapman, D. (2002). *Med. Phys.* **29**, 2216–2221.

Keyriläinen, J., Fernández, M., Fiedler, S., Bravin, A., Karjalainen-Lindsberg, M.-L., Virkkunen, P., Elo, E.-M., Tenhunen, M., Suortti, P. & Thomlinson, W. (2005). *Eur. J. Radiol.* **53**, 226–237.

Keyriläinen, J., Fernández, M. & Suortti, P. (2002). *Nucl. Instrum. Methods Phys. Res. A*, **488**, 419–427.

Khelashvili, G., Brankov, J. G., Chapman, D., Anastasio, M. A., Yang, Y., Zhong, Z. & Wernick, M. N. (2006). *Phys. Med. Biol.* **51**, 221–236.

Langford, J. I. (1978). *J. Appl. Cryst.* **11**, 10–14.

Lewis, R. A., Rogers, K. D., Hall, C. J., Towns-Andrews, E., Slawson, S., Evans, A., Pinder, S. E., Ellis, I. O., Boggis, C. R. M., Hufton, A. P. & Dance, D. R. (2000). *J. Synchrotron Rad.* **7**, 348–352.

Nesterets, Ya. I., Coan, P., Gureyev, T. E., Bravin, A., Cloetens, P. & Wilkins, S. W. (2006). *Acta Cryst.* A**62**, 296–308.

Oltulu, O., Zhong, Z., Hasnah, M., Wernick, M. N. & Chapman, D. (2003). *J. Phys. D*, **36**, 2152–2156.

Pagot, E., Cloetens, P., Fiedler, S., Bravin, A., Coan, P., Baruchel, J., Hartwig, J. & Thomlinson, W. (2003). *Appl. Phys. Lett.* **82**, 3421–3423.

Pavlov, K. M., Gureyev, T. E., Paganin, D., Nesterets, Ya. I., Kitchen, M. J., Siu, K. K. W., Gillam, J. E., Uesugi, K., Yagi, N., Morgan, M. J. & Lewis, R. A. (2005). *Nucl. Instrum. Methods Phys. Res. A*, **548**, 163–168.

Pavlov, K. M., Gureyev, T. E., Paganin, D., Nesterets, Ya. I., Morgan, M. J. & Lewis, R. A. (2004). *J. Phys. D*, **37**, 2746–2750.

Pearson, K. (1900). *Philos. Trans.* **195**, 1–47.

Press, W. H., Teukolsky, S. A., Vetterling, W. T. & Flannery, B. P. (2002). *Numerical Recipes in C++ – The Art of Scientific Computing.* Cambridge University Press.

Renier, M., Fiedler, S., Nemoz, C., Gonzalez, H., Berruyer, G. & Bravin, A. (2005). *Nucl. Instrum. Methods Phys. Res. A*, **548**, 111–115.

Rigon, L., Arfelli, F. & Menk, R.-H. (2007). *Appl. Phys. Lett.* **90**, 113102.

Rigon, L., Besch, H.-J., Arfelli, F., Menk, R.-H., Heitner, G. & Plothow-Besch, H. (2003). *J. Phys. D*, **36**, A107–A112.

Schmidt, P. W. (1991). *J. Appl. Cryst.* **24**, 414–435.

Snyder, R. L., Fiala, J. & Bungee, H. J. (1999). *Defect and Microstructure Analysis by Diffraction.* Oxford University Press.

Suortti, P., Ahtee, M. & Unonius, L. (1979). *J. Appl. Cryst.* **12**, 365–369.

Thompson, P., Cox, D. E. & Hastings, J. B. (1987). *J. Appl. Cryst.* **20**, 79–83.

Wernick, M. N., Wirjadi, O., Chapman, D., Zhong, Z., Galatsanos, N. P., Yang, Y., Brankov, J. G., Oltulu, O., Anastasio, M. A. & Muehleman, C. (2003). *Phys. Med. Biol.* **48**, 3875–3895.

Wertheim, G. K., Butler, M. A., West, K. W. & Buchanan, N. E. (1974). *Rev. Sci. Instrum.* **45**, 1369–1371.

Zhong, Z., Thomlinson, W., Chapman, D. & Sayers, D. (2000). *Nucl. Instrum. Methods Phys. Res. A*, **450**, 556–567.